



Impact of 'core-shell' mode of printing on properties of 3D binderjet printed zirconia-alumina based bioceramics



Srimanta Barui^{a,**}, Sheetal Chowdhury^a, Rajarshi Samajdar^c, Srijan Chakraborty^d,
Meeta Gavade^e, Bikramjit Basu^{a,b,*}

^a Laboratory for Biomaterials and Translational Center on Biomaterials for Orthopedic and Dental Applications, Materials Research Centre, Indian Institute of Science, Bangalore, India

^b Centre for Biosystems Science and Engineering, Indian Institute of Science, Bangalore, India

^c Department of Chemical Engineering, Institute of Chemical Technology, Mumbai, India

^d School of Mechanical Engineering, Kalinga Institute of Industrial Technology, Bhubaneswar, India

^e BVB College of Engineering and Technology, KLE Technological University, Hubli, India

ARTICLE INFO

Keywords:

3D binderjet printing
Zirconia alumina bioceramics
Acrylic binder
Core-shell saturation
Micro-CT
Weibull modulus

ABSTRACT

3D binderjet printing of bioceramics remained a major challenge, and powder specific-binder development and processing strategies still follow certain 'black box' approaches. In this study, for the first time, we report the efficacy of an acrylic based proprietary binder system to 3D print zirconia based bioceramics. Machine limited 'core-shell' mode of binder deposition resulted in heterogeneous distribution in particle arrangement from 'shell' to 'core', with higher binder saturation at the 'shell' region and less saturation at the 'core'. A series of post-processing strategies like 'presintering – salt infiltration – phase conversion – final sintering', post-printing binder infiltration etc. were adapted to develop 3YSZ alone or together with ZrSiO₄ or Al₂O₃, although with limited success. Despite poor strength properties (compressive/tensile/flexural), the acceptable strength reliability with modest Weibull modulus ($m \approx 5-9$) was obtained in post-processed ceramics. While explaining the microstructure-property correlations, the contributions of different powder modification strategies and novel processing steps ('dual powder deposition' for non-macroporous powder bed) are discussed in particular reference to the porous architecture formed in 2D space or 3D volume, as investigated using SEM or micro-computed tomography.

1. Introduction

Additive manufacturing captivated the attention of the biomedical engineering community in terms of the potentiality to produce biologically complex architectures, since the last two decades [1–6]. Although it evolved in the early 1980's as a rapid-prototyping technique, additive manufacturing of ceramics remained a challenging task. Zirconia-based biomaterials were introduced more than 30 years ago and received more attention [7] due to the phase transformation toughening. Among bioceramics, ZrO₂ is regarded as a bioinert, material which does not participate actively with the host tissue in the cellular and physiological functionalities [8]. The biomedical grade zirconia exhibits the best mechanical properties among oxide bioceramics, e.g. high fracture

toughness, flexural and compressive strength. Due to synergism among these properties, zirconia is also known as 'ceramic steel'. Zirconia based dental implants and zirconia toughened alumina for articulating prosthesis are a few successful examples of partially or fully stabilised (CaO, MgO, Y₂O₃ and CeO₂ as stabilisers) zirconia, which have been clinically used.

Various attempts to fabricate zirconia-based design specific/patient specific implants/scaffolds using laser/electron beam/extrusion based additive manufacturing technologies are reported in the literature, since the early 1990's [9]. Using a novel ceramic on-demand extrusion (CODE) set up, Ghazanfari et al. printed fully stabilised zirconia (8 mol% yttria stabilised), dispersed in aqueous media using a surfactant with 50% zirconia loading [10]. A volumetric shrinkage of ~53% was recorded

* Joint corresponding author: Laboratory for Biomaterials and Translational Center on Biomaterials for Orthopedic and Dental Applications, Materials Research Centre, Indian Institute of Science, Bangalore, India

** Corresponding author.

E-mail addresses: srimantab@iisc.ac.in (S. Barui), bikram@iisc.ac.in (B. Basu).

<https://doi.org/10.1016/j.oceram.2020.100026>

Received 11 July 2020; Received in revised form 5 October 2020; Accepted 8 October 2020

Available online 15 October 2020

2666-5395/© 2020 The Authors. Published by Elsevier Ltd on behalf of European Ceramic Society. This is an open access article under the CC BY-NC-ND license

(<http://creativecommons.org/licenses/by-nc-nd/4.0/>).

after sintering. Shao et al. used a 3D gel printing based extrusion assembly to print 2-hydroxyethyl methacrylate based gel, loaded with 50% volume of zirconia [11]. A relative density of 97.6% was achieved after sintering. Scheithauer et al. used a thermoplastic extrusion based 3D printer to print a pre-formulated blend of paraffin wax and zirconia powders, followed by debinding and sintering to achieve more than 99% relative density [12]. In order to avoid the thermal stress-oriented crack formation, Shahzad et al. used indirect selective laser sintering to 3D print a pre-formulated thermoplastic-zirconia blended powder with a relative density of 36% [13]. A post-printing infiltration with zirconia slurry (30 vol% loading) could increase the density up to 54% and after warm isostatic pressing and sintering, the density increased up to 90%. Wilkes et al. used powder bed based direct selective laser melting to manufacture a eutectic composition of zirconia-alumina with complex architectures [14]. The cracking in the as-printed objects were observed, where no pre-heating was used to treat the printable powders. Fan et al. used laser engineered net shaping (LENS) to fabricate fully yttria stabilised zirconia and the printing could induce phase transformations to tetragonal and cubic phases [15]. 98.7% relative density was achieved and the microcracking could be controlled by judiciously choosing the laser power. In another work, Yan employed a direct laser deposition based (LENS type) printing set up to 3D print a eutectic composition of $ZrO_2 - Al_2O_3$ system [16]. Using an ultrasound attachment during printing, the porosity could be minimised in as-printed highly dense ceramics (~99.9% relative density). He et al. fabricated complex shaped zirconia parts, using digital light processing (DLP) based stereolithography (SLA), with ~35% and 97% relative density [17]. In another work, Wu et al. used SLA methodology to fabricate dense zirconia toughened alumina (ZTA) by selectively curing layers of ceramic loaded resins with photoinitiator and the printed ZTA had the final relative density of ~99.5% [18].

Binderjet printing of ceramics is a relatively newer additive manufacturing technique (in the late '90s) compared to SLA, micro-extrusion, etc., which is essentially a powder bed based room temperature fabrication process [19–21]. As a result, apart from temperature sensitive biomaterials, a wide spectrum of chemically modified materials also can be fabricated using this processing route. In a recently published paper from our group, the efficacy of a proprietary acrylic based ink/binder in binderjet printing of metallic biomaterial (Ti-6Al-4V) is reported [22]. In this study, the printability of ZrO_2 based bioceramics with same binder system is investigated. The limited mechanical properties obtained are explained in terms of the 'default core-shell' mode of printing using the commercial binderjet printer. At the end, a series of troubleshooting methodologies and comprehensive solutions are also suggested to overcome these limitations.

2. Materials and methods

2.1. Powder preparation and modification

Three compositions of bioceramics powders were considered for binderjet printing, 1) pristine 3 mol% yttria-stabilised zirconia (3YSZ), 2) zirconia (12% wt/wt)-alumina blend doped with magnesia (1500 ppm, sintering aid) and 3) zirconium silicate (zircon, 25% wt/wt)-3YSZ blend. These powders were procured from Mincometsal, Bangalore, India. Zircon-zirconia and zirconia-alumina powder mixtures (magnesia added) were blended in an in-house fabricated horizontal jar mill for 1.0–1.25 h for homogeneous blending. The pristine zirconia and alumina-zirconia blended powders were mixed with 15% (wt/wt) ammonium persulfate (APS), while the zircon-zirconia blend was modified using 5% (wt/wt) APS using the same horizontal jar mill. After blending, all powders were passed through a sieve of mesh size 100 μ m.

The APS modified pristine zirconia and zirconia-alumina powder blend were treated with a controlled humidification step to incorporate moisture on the surface of the ceramics particles in order to enhance the cohesive interaction among powder particles to obtain a good bed

packing during printing. To allow the steam to pass through the powder particles, the powder container was covered with a series of coarse sieves (100–300 μ m) veiled with dry tissue paper (to avoid direct contact of condensed water vapor with the powder) and placed in an autoclave at 80 °C for 30 min. The reactivity of the premixed APS after autoclaving was checked by adding a few drops of acrylic binder with a pinch of the autoclaved powder blend to confirm the instant adhesiveness ('binder check'). Due to the strategic blending with zirconium silicate, the cohesiveness among particles was achieved and no further humidification was required for zircon-zirconia powder blend. The absence of moisture allowed significantly less amount of APS (5% wt/wt, in contrast with 15% wt/wt for 'humidified' pristine zirconia and alumina/zirconia blend) to sufficiently modify the zircon-zirconia powder blend with high shelf-life (≥ 1 month).

2.2. Binder preparation

As part of the binder formulation, 22% (wt/vol) acrylamide (SDFCL, Mumbai, India) was dissolved in deionised water, supplemented with 1.0–2.0% (vol/vol) N,N,N',N'-tetramethylethane-1,2-diamine (TEMED, Spectrochem, Mumbai, India) as free radical stabiliser. The aqueous solution was magnetically stirred for 10–15 min to obtain a clear solution, followed by filtration through Whatman 40 filter paper.

The stepwise preparation of the binder used to 3D binderjet print bioceramics is identical as that described in our previous work [22]. The composition and physical properties (viscosity, surface tension, Oh, We, Re) of the binder/ink are provided in the supplementary section (Table S1), which were maintained in 3D binderjet powder printing of Ti-6Al-4V²².

2.3. 3D CAD preparation and binderjet printing of bioceramic powders

A number of coupon bioceramic samples were printed, post-processed, and evaluated in this study. In particular, the cylinders (14 mm \times 10 mm, $h \times d$) for compressive strength measurement, rectangular bars (6 mm \times 6 mm \times 12 mm, $b \times d \times l$) for flexural strength measurement, and circular disks (20 mm \times 7 mm, $d \times h$) for tensile strength measurements (via diametral compression tests) were designed in Solidworks™. A commercially available 3D binderjet printer (Projet 460 plus, 3D Systems, Germany) was customised to 3D binderjet print the ceramic blended powders. After bypassing all the sensors to make the printer 'interactive', the binder/ink line is connected with the printing gantry and the manually purged (with acrylic ink/binder) printhead is placed on the binder line septum. The schematic of the printing methodology is represented in Fig. 1.

The bioceramic powder blends were deposited on the 'static' bed, followed by spreading the powder homogeneously on the build bed using a spreader roller. Being porous in nature, another round of loose powder sprinkling was applied on the as-spread bed and when the next powder layer was deposited, it resulted in a smooth layer for the print. The methodology is shown in Figure S1.

An identical value of 100–110% saturation was maintained throughout the print. Although the core and shell saturation were kept identical by input, the binder concentration, by default was segregated (machine limited), resulting in higher concentration at the shell and lighter deposition at the core. This led to the heterogeneous structural properties in the as-printed architectures, which were unavoidable (Fig. 2). The issue of segregation remained unaltered even if the core saturation is doubled than the shell region in the slicing software. It was observed from the slicing software that, after 20–25% printing, the core region appeared in the structure. In other words, the thickness of the shell is around 20–25% of the major dimensions (height, diameter, length, breadth, etc. depending on the structure) of the part. The generation-wise strategies of different powder modifications are demonstrated in Fig. 3. The corresponding challenges and troubleshooting strategies will fall in place in the upcoming sections.

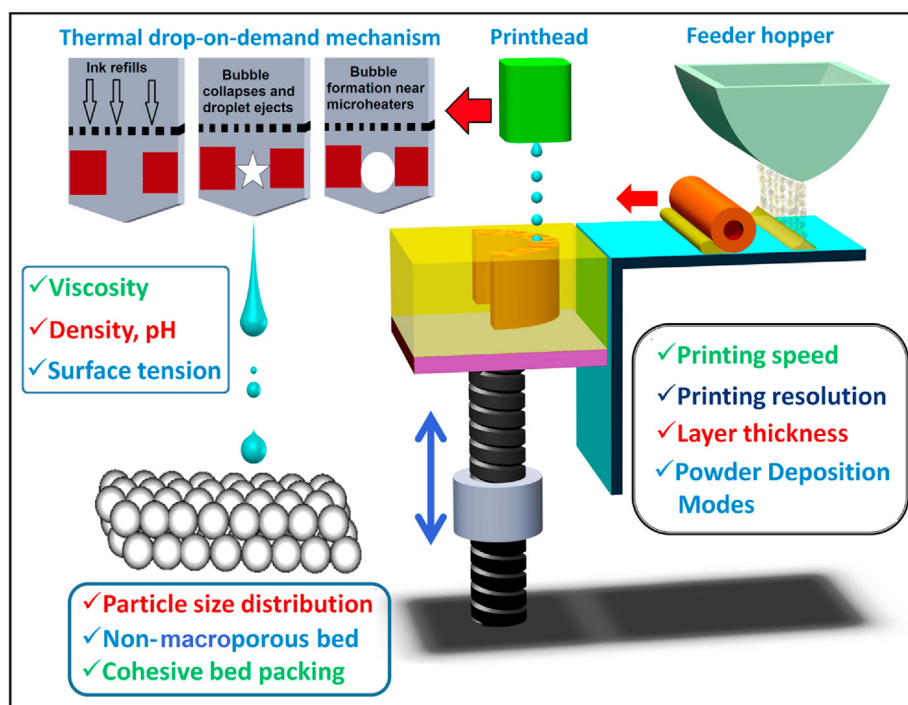


Fig. 1. Schematic representation of 3D binderjet printing of zirconia based bioceramics with single build bed and static feeder bed.

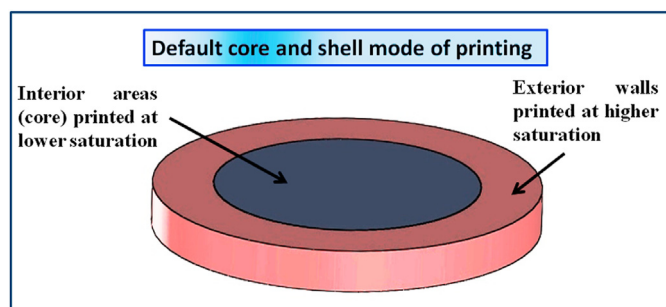


Fig. 2. Projet 460 plus binderjet printer default 'core-shell' mode of printing leading to binder concentration (saturation) segregation (unavoidable). This potentially gives rise to structural inhomogeneity which is detrimental for mechanical properties.

2.4. Post-processing

2.4.1. Part removal and depowdering

Once the printing is over, the excess powder outside the printing area is recovered and the build platform with the printed objects, covered in loose powder pool, is taken away. The printed parts were placed inside a hot air oven (60–70 °C) overnight to ensure complete drying of the polymeric binder and achieving tenacity in the green bodies. After this, the loose powder is recycled and sieved again to reuse. The obtained green bodies are further subjected to post-printing strengthening. One of the strategies to strengthen the as-printed zircon-zirconia architectures was "pre-sintering – zirconium salt solution infiltration – phase conversion to zirconia – full sintering", while multistage sintering was adopted to strengthen the zirconia-alumina and pure zirconia architectures.

2.4.2. Presintering-infiltration-phase conversion-sintering based strengthening of binderjet printed zircon-zirconia

The depowdered 3D architectures (zircon-zirconia) were pre-sintered

for 2 h at a relatively lower temperature than the sintering temperature, e.g. 1000 °C–1200 °C. After cooling to room temperature, the green-bodies gained structural stability and were kept inside a round bottom flask, followed by evacuating with the help of a rotary vacuum pump for at least 30 min. A saturated solution of zirconium oxychloride ($ZrOCl_2 \cdot 8H_2O$) was prepared and transferred in the flask under negative pressure to infiltrate the microporous architectures. After retaining it for 20–30 min in the solution for complete infiltration, the infiltrated structures were taken away from the solution and dried overnight. The infiltrated and dried parts were heated at 400–450 °C to convert the zirconyl chloride to tetragonal zirconia. The cycle of 'infiltration-drying-phase conversion' was repeated for 3–4 times in order to fill up all the possible micropores, inside the structures. After each conversion, the increments in the weight (zirconia formation in the micropores) were monitored. After the final cycle, the architectures were finally sintered at 1450 °C for 2.5 h–3 h. A homogeneous shrinkage of 20–22% was observed after final sintering.

2.4.3. Multistage sintering of zirconia-alumina and pure zirconia based as-printed architectures

Two different post-printing heat treatment protocols were followed for zirconia-alumina and zirconia based 3D binderjet printed architectures. The green bodies of zirconia-alumina were sintered in two subsequent stages. In the first stage, the green bodies were sintered in a muffle furnace (Carbolite, Verder Scientific, Hyderabad, India) at 1450 °C for 4 h at a ramp rate of 10 °C/min. The partially sintered bodies were furnace cooled and in the second stage, were kept in a glass wool insulated tubular furnace (Nabertherm, Lilienthal, Germany), where the temperature was increased at a rate of 10 °C/min till 1000 °C. This step was followed by a delayed ramp rate of 3 °C/min up to 1600 °C. After dwelling at 1600 °C for 10 h, the architectures were furnace cooled. On the other hand, the as-printed zirconia green bodies were sintered in three stages. In each stage, the furnace temperature was increased from room temperature up to the sintering temperatures (1200 °C, 1350 °C, 1450 °C) at a heating rate of 10 °C/min and soaked for 4 h at the final temperature, followed by furnace cooling. All the sintering profiles are shown in Fig. 4.

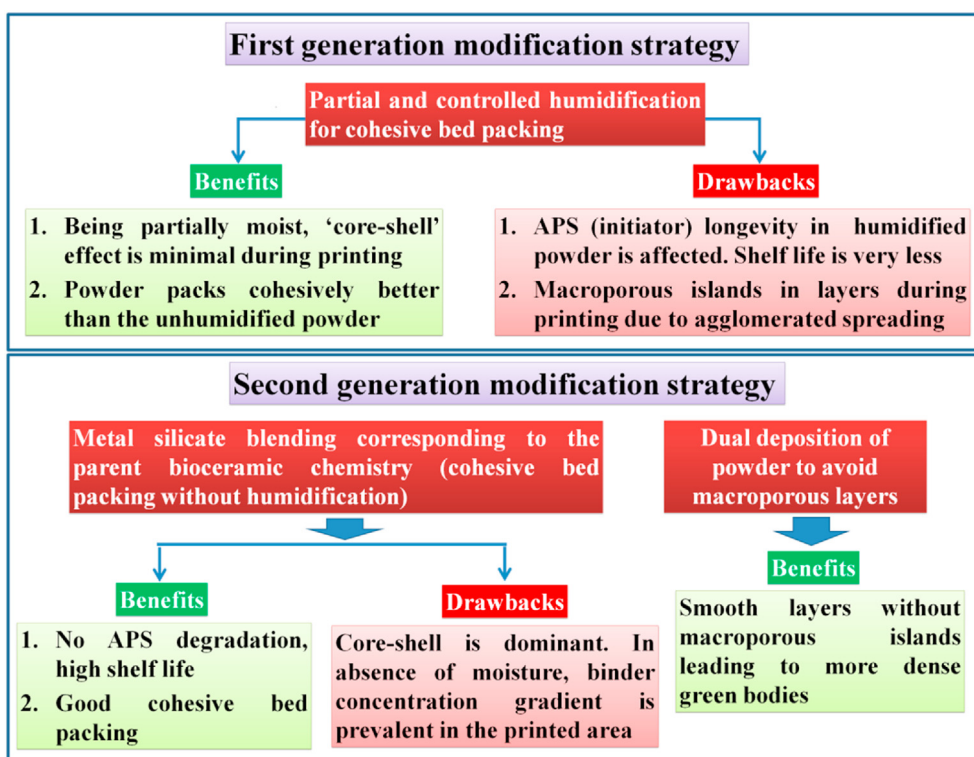


Fig. 3. Generation-wise bioceramic powder modification strategies to make them printable by virtue of incorporating the cohesive interactions among the powder particles for good bed packing during layer spread.

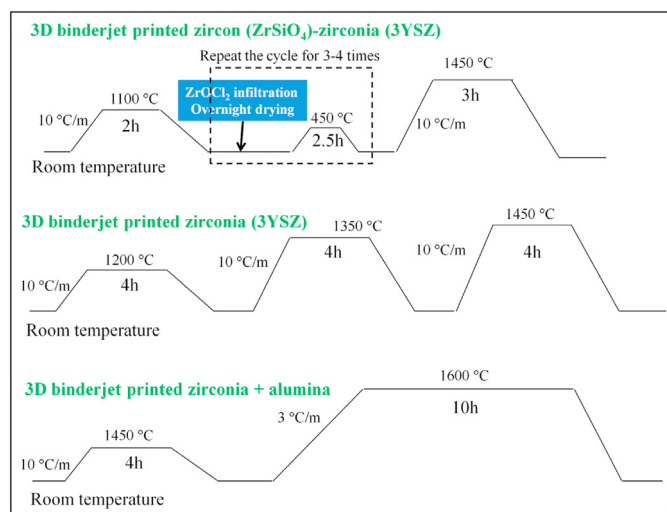


Fig. 4. Post-processing and sintering profiles of zirconia (3YSZ), zircon-zirconia and zirconia-alumina based as-binderjet printed architectures. (Soaking temperature/time, ramping and cooling slopes not to scale from the line diagrams).

2.4.4. Phase assemblage, microstructure, and mechanical properties

X-ray diffractometer (X' Pert Pro, PANalytical, Netherlands) was used to investigate the phase assemblage in all the powders as well as specimens under consideration. All the samples were scanned for 2θ in the range of 20° – 90° with a scan rate of $0.06^\circ/\text{sec}$ using $\text{Cu K}\alpha$ radiation of wavelength 1.5418 \AA . The printed-sintered zirconia and ZTA based microporous architectures were thermally etched to investigate the grain structures. Zirconia and ZTA samples were heated to 1200°C in a muffle furnace at a heating rate of $20^\circ\text{C}/\text{min}$, followed by a hold for 30 min. A scanning electron microscope (Zeiss, Oberkochen, Germany) was used at an accelerating voltage of 20 kV (SE2 mode) to probe the as-etched

microstructure. Prior to studying under SEM, all the 3D architectures were gold coated for $\sim 1.0 \text{ min}$ to make the surface electronically conducting.

Microcomputed tomography (VersaXRM-500, Xradia, Zeiss, Germany) analysis for the bioceramics microporous scaffolds (diameter 5–6 mm, 10 mm height) were carried out to qualitatively monitor the evolution of 3D microstructure after the particular post-processing treatments (infiltration, phase conversion, multi-heat treatments, etc.). Transmitted X-Ray intensity was maintained >5000 at 140 kV energy and 10 W power using 4X objective and different exposure times (3–5 s) to obtain high resolution scan images. In each scan, 1601 projection images were acquired with voxel size of $3.5 \mu\text{m}$ and binning 2. The 2D tomogram slices were reconstructed using the manufacturer proprietary XRM Reconstructor (Xradia, Zeiss, Germany) to obtain the corresponding virtual 3D scanned data.

The density of the post-processed parts was measured using Archimedes principle. To block the surface and 3D interconnected pores from water infiltration during bulk/apparent density measurement, a very thin coating of silicone grease was applied on the surfaces of the 3D printed-sintered and post-processed parts. The shrinkage analysis was carried out by normalising the final dimensions after sintering and/or post-processing with the initial green body dimensions.

The mechanical properties of the 3D printed and sintered/post-processed architectures were assessed using a table top micro-UTM (MultiTest 10-i, Mecmesin, UK) with a 5 kN load cell and 1 mm/min cross-head speed for different test conformations (compression, diametral compression test, and 3-point bending). For flexural tests, a span length of 12 mm was used. Weakest link fracture statistics was adapted to analyse the strength reliabilities (Weibull modulus) of various architectures in different loading conditions (compressive, diametral compressive, and flexural). The theory for weakest link fracture statistics for strength reliability analysis can be found in our previous work [22].

3. Results

3.1. Powder bed preparation and 3D binderjet printing

The qualitative bed packing of humidified (pristine zirconia and zirconia (12% wt/wt)–alumina blend) and silicate blended powder (zirconia:zircon, 3:1 wt/wt added with APS) was stable in each deposited layer during an uninterrupted session of 3D printing, aided with dual deposited smooth layers. All the as-fabricated architectures maintained very good geometric tolerance and as-printed ‘green strength’ for handling. The examples of the as-printed and sintered bioceramic architectures are shown in Fig. 5. Very fine cracks were observed on the surface of the sintered objects. At least 16 samples for each category were printed and post-processed.

3.2. Conversion of zirconia from zirconyl chloride *in situ*

The dynamic weight gains by the microporous scaffolds were significant and after each ‘vacuum infiltration-drying-conversion’ cycle, the weight increased in a sluggish manner. At some point, after a finite number of cycles, the graph should exhibit a plateau implying that all the micropores are filled with zirconia. In the current experiment, due to time limitation, repetition of the cycle until the attainment of the plateau was not explored. Fig. 6 shows the strategic zirconia conversions *in situ* in the microporous scaffolds. For the reproducibility in the results, four random samples initially weighing 1.14 g, 1.05 g, 1.08 g, and 1.05 g respectively, were considered. At the end of 1st vacuum infiltration-drying-conversion cycle, the weights gained by the four samples were 21.05%, 20.95%, 21.29%, and 20.95% respectively. At the end of 2nd vacuum infiltration-drying-conversion cycle, the weight of the samples further increased by 13.76%, 14.96%, 14.19%, and 14.17% respectively; whereas after 3rd cycle, the weights increased by 12.19%, 10.95%, 10.96%, and 10.34%, respectively. This indicates the gradual filling up of the micropores inside the bodies in each cycle, leading to a progressive decrement in the salt intake followed by thermal conversion to zirconia.

3.3. Phase assemblage and microstructure

Fig. 7a–b represents the phase assemblages of all the precursor powders and sintered ceramics in zircon-zirconia and zirconia-alumina system. Fig. 7a showed that even at very high temperature (1450 °C), zirconium silicate was stable, which was endorsed by the identical peak positions with the as-received powder. This result provided the assurance of the strategy to blend zirconium silicate with zirconia in order to achieve cohesive bed packing. Further, the converted zirconia from heat treated zirconyl chloride salt showcased the prevalence of tetragonal

zirconia in the microstructure, as evident in the characteristic peaks in the 2 θ range of 28°–32°.

In the sintered powder blend, the combination of all the characteristic peaks of zirconia and zircon was present. As-expected, tetragonal zirconia (converted from zirconium oxychloride salt) transformed to monoclinic phase in the sintered ZrO₂ (see Figure S2).

Fig. 7b shows the phase assemblages of α -alumina, 3 mol% yttria stabilised zirconia (as-received), α -alumina and 3YSZ (12% wt/wt) powder mixture, sintered zirconia, and sintered zirconia toughened alumina. The XRD pattern of zirconia powders represents the mixture of tetragonal (t-Z) and monoclinic (m-Z) phases. The high intensity peak at 2 θ ~30.2° refers to the characteristics peak of t-ZrO₂. A similar pattern for sintered zirconia indicates the phase purity after sintering. The pattern for alumina and zirconia powder mixture showed the existence of both the phases, where the intensities of t-ZrO₂ and m-ZrO₂ were less due to the presence of a relatively lower amount (12% w/w) of zirconia in the mixture. XRD analysis of sintered zirconia toughened alumina indicates the phase stability, post-sintering.

The microstructure of binderjet printed-sintered zirconia toughened alumina and zirconia are shown in Fig. 8. The highly interconnected microporosities dominate the microstructure (Fig. 8a and c), irrespective of the composition of the starting powder mix. Higher magnification images demonstrate the thermally etched grains of ZTA and zirconia (Fig. 8b and d), where the randomly distributed finer grains of zirconia are found to be embedded in the alumina matrix (yellow encircled). Fig. 8d represents homogeneously distributed almost equiaxed and submicron sized grains of zirconia. It is worthwhile to note that, the compact grain structures are the surface characteristics of the thin ‘shell’ region of the microporous scaffolds, which is not the representative of the bulk structure, mostly contributed by the loosely bonded ‘core’.

While the denser microstructure of the ‘shell’ was observed from the SEM images of 3YSZ and ZTA, the high resolution micro-CT scan captured the loosely bonded 3D microstructures of the ‘core’ regions of the printed-post processed zirconia-zircon architectures. Significantly inconsistent microstructure demonstrated least densification in the ‘core’ regions. Multiple cracks are observed in different architectures after ‘presintering-infiltration-conversion-final sintering’ cycle. Although the particles arrangements were found to be inconsistent with high porosity, cracks were not found in case of the ‘presintered-infiltrated-converted for 3 times’ samples (Fig. 9a–b).

After the final sintering at 1450 °C, the microstructure became denser (visually from the micro-CT images) compared to the 1200 °C pre-sintered microstructure, but at the expense of the crack formations (Fig. 9d–e). These cracks in the poorly dense ‘core’ region actively deteriorated the mechanical properties of the microporous scaffolds as more than 80% of the volume of the 3D printed objects are contributed by the ‘core’ region.

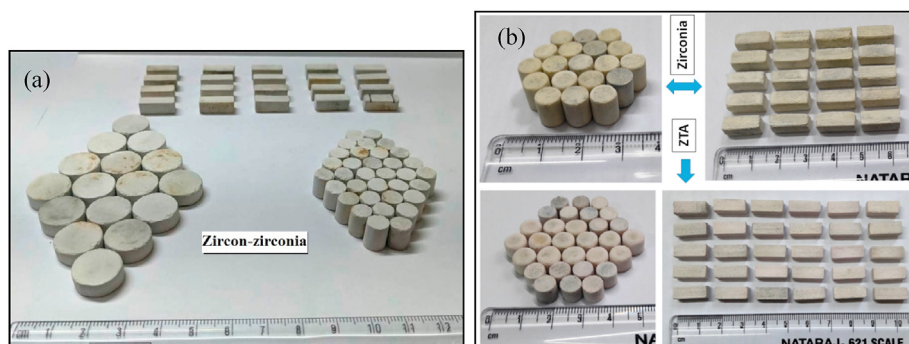


Fig. 5. Binderjet printed-sintered bioceramics architectures. (a) Zircon-zirconia (1:3) based architectures, flexural bars, diametral compressive test disks (and compressive test cylinders); (b) top row: printed-sintered zirconia 3D structures for flexural and compression tests, bottom row: printed-sintered zirconia toughened alumina 3D structures for flexural and compression tests respectively. The lead graduations in the scales are in cm.

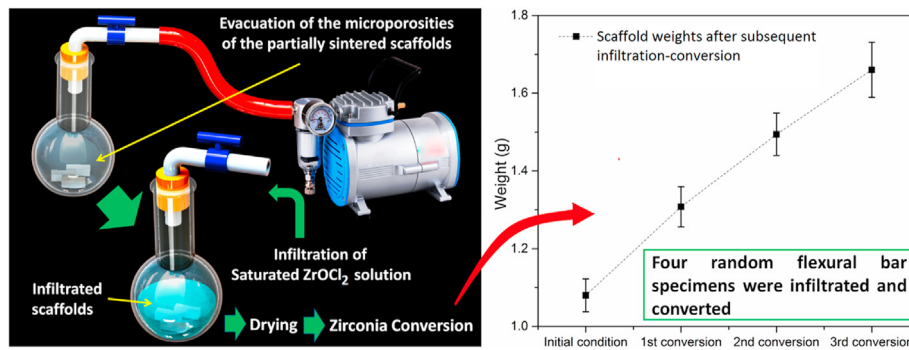


Fig. 6. An attempt to evacuate the trapped air in the microporosities with the help of the rotary pump to enhance the infiltration. Conversion of tetragonal zirconia from infiltrated zirconyl chloride inside the microporous scaffolds *in situ*. As a result, in each cycle infiltration and conversion, the weights of the scaffolds increase (average of four random samples were considered).

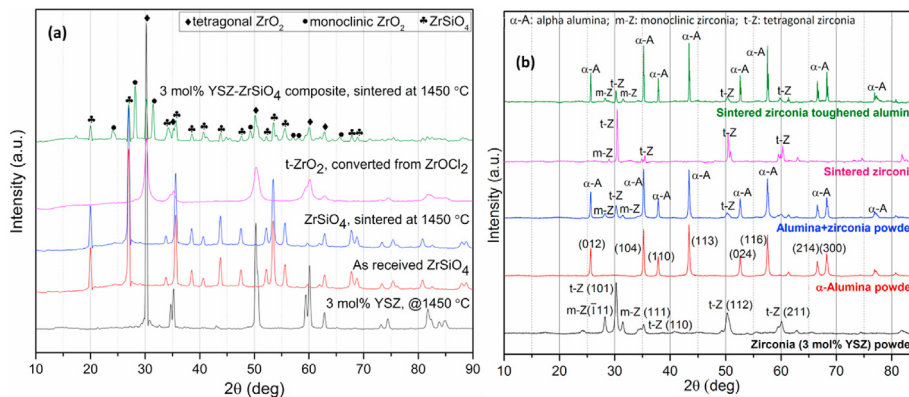


Fig. 7. Phase assemblage of (a) all the as-received powders (zircon and zirconia) and sintered 3D binderjet printed structures along with phase transformed zirconia; (b) as-received 3YSZ and α-alumina powder and their prescribed mixtures. The individual phases were stable even after 3D binderjet printing and subsequent high temperature sintering.

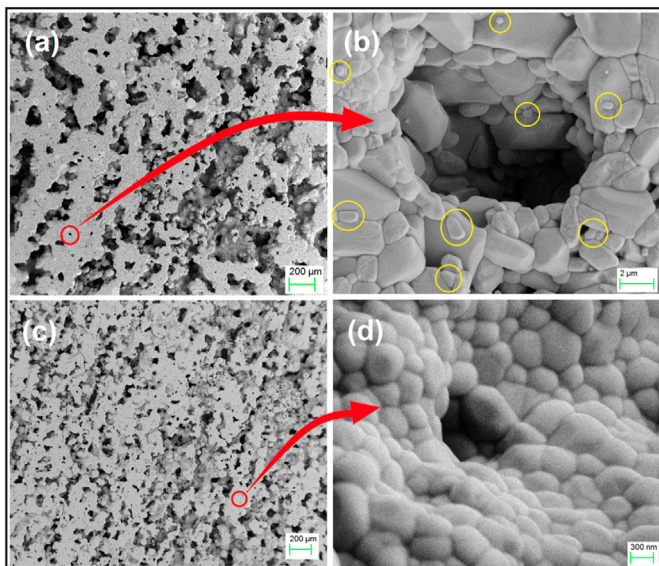


Fig. 8. Binderjet printed-sintered-thermal etched surface morphology of zirconia (3YSZ) and ZTA. Lower magnification images (a & c) exhibit the highly interconnected microporosities in the microstructures of both printed-sintered zirconia and ZTA. Higher magnification images (b and d) demonstrate the thermally etched grains of ZTA and zirconia respectively. Smaller sized randomly distributed zirconia grains are visible in the alumina matrix in ZTA microstructure (encircled).

3.4. Post-sintering shrinkage and mechanical properties

The accounts of the post-sintering shrinkage, apparent and true densities are exhibited in Table 1. Homogeneous shrinkages were observed in all binderjet printed-sintered parts, irrespective of the structural geometries and composition of the precursor materials.

An average compressive strength of 6.8 ± 1.6 MPa and tensile strength of 1.2 ± 0.3 MPa were recorded with binderjet printed-sintered zircon-zirconia based cylinders. A trend of progressive failure in the microporous cylindrical specimens was noticed during the compression tests (Figure S3). The detachment of the shell from the core under compressive stress followed by lateral bulging attributes to the adverse effect of the differently densified 'shell-core' regions on the mechanical properties (Fig. 10a). As expected, discrete cracks propagating through the diameter were observed in the failed specimens after diametral compression tests (Fig. 10b). Surprisingly and counter-intuitively, higher flexural strength (12 ± 2.1 MPa) with respect to the compressive strength (6.8 ± 1.6 MPa) was recorded. The hypothesis for this anomalous behaviour will be discussed later.

The weakest link fracture statistics were adapted to calculate the Weibull modulus from the flexural and compressive strength measurements of 3D binderjet printed-sintered architectures ($n \geq 16$). Fig. 11 represents all the strength reliability plots. The mean mechanical properties (compressive and flexural) of different architectures along with the corresponding Weibull modulus are provided in Table 2.

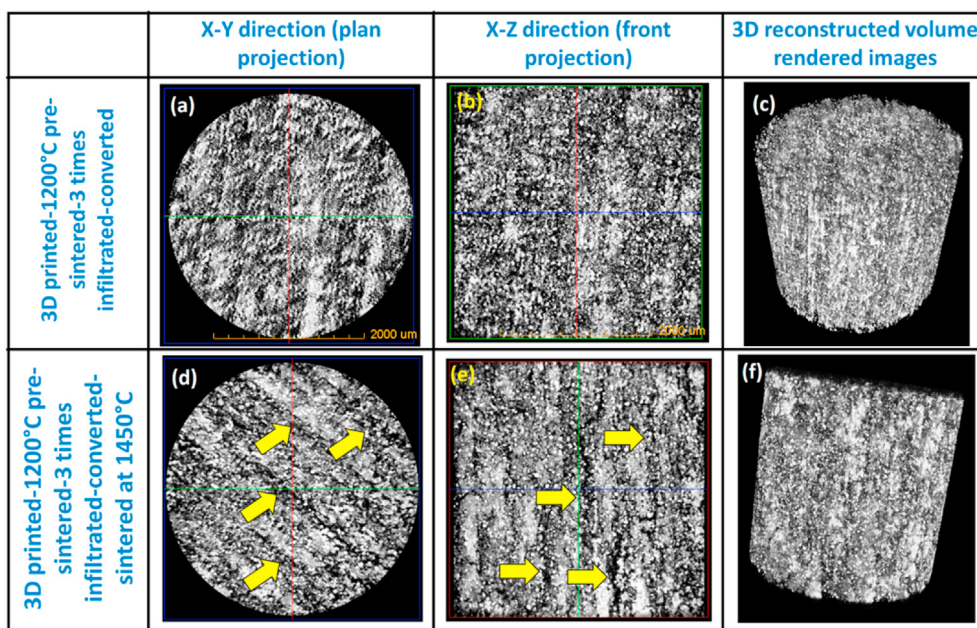


Fig. 9. High resolution micro-CT scan images showing the ‘core’ microstructure and the evolutions of cracks based on different ‘post-processing-heat treatment’ combinations. The adverse effect of ‘infiltration-conversion-full sintering’, intended to fill up the pores is witnessed which contributed in cracks (indicated in yellow) which may be due to the high mismatch in the densities of ‘core’ and ‘shell’ and the formation of monoclinic zirconia.

Table 1

As sintered and/or post processed shrinkages and densities of various bioceramic architectures.

	Shrinkage (%)	Apparent density (g/cc)	True density (g/cc)
Zirconia	29.5	3.4	6.03
ZTA	26.6	2.52	4.1
Zircon-zirconia	21.2	3.22	5.34

4. Discussion

Apart from stereolithography, selective laser sintering, or micro-extrusion based manufacturing approaches, parallel endeavors reported to manufacture zirconia based bioceramics using binderjet/direct inkjet printing methodologies. Direct inkjet printing was predominantly used to manufacture zirconia/alumina bioceramics. For example, Watjen et al. used the direct inkjet printing methodology to fabricate zirconia and alumina (separately, both 21 vol%) laden ink to fabricate on-demand complex architectures and ~97% relative density was recorded for zirconia [23]. Ebert et al. manufactured zirconia (3YSZ)-based dental prosthesis using direct inkjet printing (drop-on-demand based), where a post-sintering isotropic shrinkage of 20% was measured while achieving ~97% relative density [24]. In another work, Ozkol et al. used a similar type of direct inkjet printing setup to print 3YSZ for dental restoration [25]. Ramakrishnan et al. simulated the drop formation and spread in direct ceramic inkjet printing. They established the influence of several factors like the dispersants, pH, and ceramic loading amount on the drop formation during inkjet printing. The same group also discussed the impact of viscosity, tail formation, and drop diameter on the ink spreading on a substrate [26]. In another relevant study, Dou et al. established the temperature-dependent coffee staining of deposited zirconia based ink from a direct inkjet printer (piezoelectric), resulting from the concentration-based ceramic particle segregation during drying [27]. On the other hand, Budding et al. adapted binderjet printing to 3D print zirconia and alumina blend, using a customized powder-bed based binderjet printing set up and a commercial binder (ZB61) [28]. In another recent work of 3YSZ binderjetting, Huang et al. used a particle

free inorganic colloid binder to investigate the efficacy of *in situ* zirconia formation during heat treatment and filling up of pore and enhanced densification [29]. When compared with the ‘direct inkjet printing’ and ‘extrusion’ based printing methodologies, in the literature, there prevails a clear gap in the exploration and satisfactory knowledge-base in the area of binderjet printing of zirconia/alumina based bioceramics. In the reported studies of powder bed based 3D printing of zirconia/alumina based bioceramics, researchers have either used machine proprietary binder or starch based adhesive binder so far.

“Morning shows the day” is suitably applicable in 3D binderjet printing of ceramics, where the extent of the compaction of powder particles in ‘green body’ dictates the final density after post-processing. In the case of binderjet printing of powder materials, an extremely narrow window for the scope of powder compaction exists during fabrication. This happens during the powder spreading by the roller, leading to the unavoidable high porosity (~50%) in as-printed structures [30–33]. Pressureless sintering, as followed to densify the as-printed architectures, is not capable to reduce the porosity significantly. For example, the reduction of bulk porosity to 10% in sintered ceramics, starting at 50% green porosity is of great challenge through pressureless sintering. If the as-deposited powder particles in a layer do not bind intimately and homogeneously with each other during printing, it is not possible to obtain a final 3D architecture with biomedically reliable strength properties after post-processing and/or sintering. In a nutshell, it is of primary importance to have less porous and well bonded as-printed body. In this section, several attempts to address the limitations are made and innovative suggestions for troubleshooting are discussed.

4.1. Powder characteristics and modification strategies for binderjet printing

Several attempts to prepare/modify bioceramic powders for optimised binderjet printability were made and the same is represented illustratively in Fig. 3, generation-wise. While it was observed that partial moisturisation of the APS modified powder could contribute to the printability in terms of cohesive particle interactions, the stability of the APS in the powder was limited due to the sensitivity of APS towards moisture leading to significantly less ‘shelf life’ (maximum 1 day). Apart

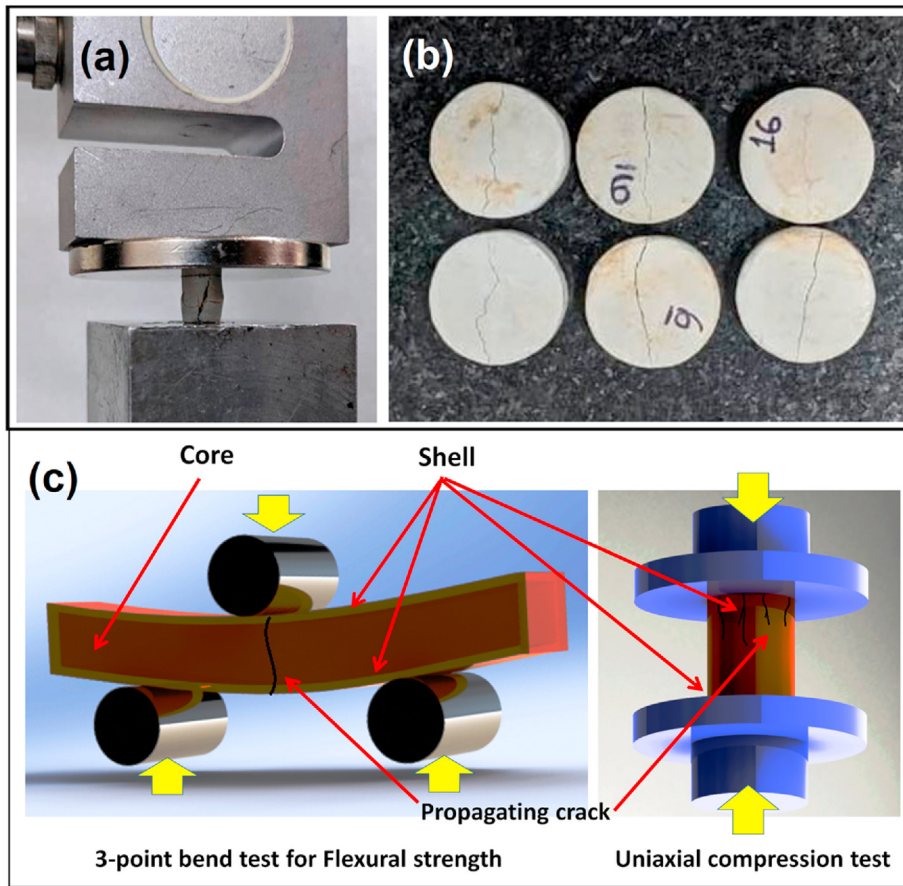


Fig. 10. Modes of failures in different tests. (a) core-shell separation and progressive failure in compression test, (b) crack propagations in the fractured disks under diametral compressive tests (for tensile strength); (c) The higher flexural strength compared to the compressive strength can be explained from the fact that a crack has to pass two shells (top and bottom) to fracture an object in a 3-point bending experiment while in compression test, when any of the top/bottom shells breaks, there is no supporting candidate to withstand the load and the body collapses in a relatively lower load.

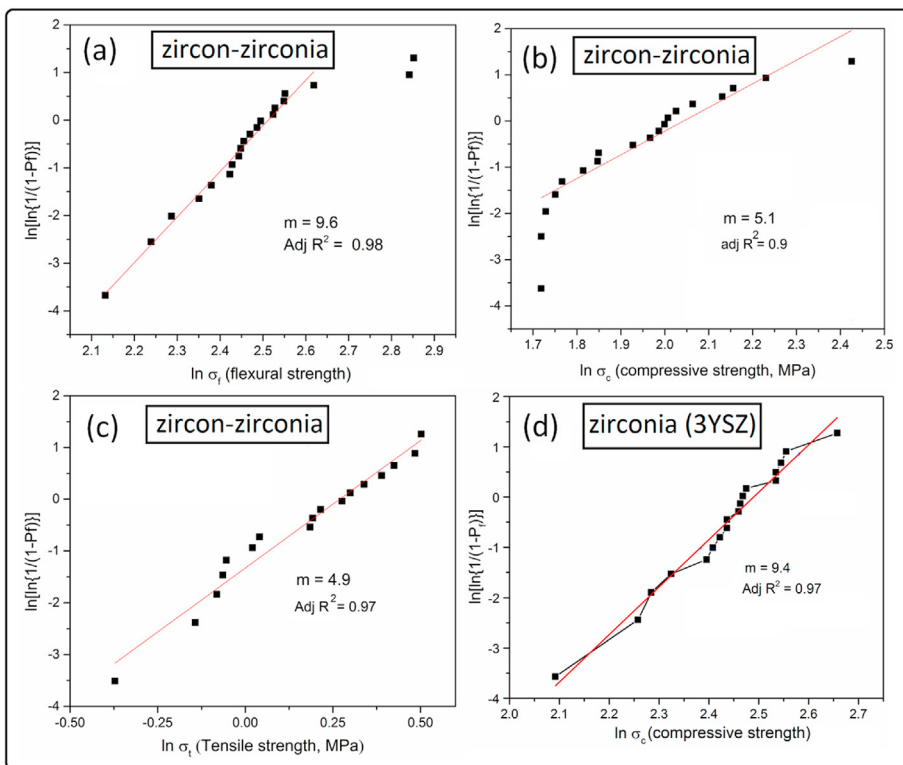


Fig. 11. Weakest link fracture statistics-based analysis of the flexural and compressive strength data using Weibull theory to assess the strength reliability of 3D binderjet printed and sintered zirconia based bioceramics. Weibull modulus plots for binderjet printed-sintered zircon-zirconia based bioceramic materials (a–c). The higher Weibull modulus and mean value of flexural strength compared to tensile strength measured via diametral compression test and compressive strengths are explained based on the typical core-shell structure; comparatively higher compressive strength and Weibull modulus of zirconia based cylinders are expected to be originated from different powder preparation methodology (humidification) and less core-shell segregation (d).

Table 2

Summary of the mechanical properties, statistical strength reliabilities, and porosities of binderjet printed-sintered and/or post-processed zirconia based bioceramics based 3D architectures.

(n ≥ 16)	3D binderjet printed architectures (disks, bars, and cylinders)				
	Zircon-zirconia based bioceramics			Zirconia	ZTA
	Flexural strength	Compressive strength	Tensile strength	Compressive strength	Flexural strength
Mean ± SD (MPa)	12 ± 2.1	6.8 ± 1.6	1.2 ± 0.3	11.4 ± 1.4	37.5 ± 6.2
Weibull modulus (m)	9.6	5.1	4.9	9.4	6.8 (plot not shown)
Volume porosity (%)	40.8			44	37.6

from this, during the autoclave treatment, the APS can degrade if the temperature rises to more than 90 °C. Alternatively, it is not possible to modify moisturised powders and subsequently sieve it due to strong agglomeration formation. It was found that up to 10% APS addition with the bioceramic powder, after humidification in autoclave, it fully degraded and the instant polymerisation was absent during 'binder check'. In order to compensate for the degradation, the optimal APS content to modify the powders was set to ~15%, which is significantly high. Although the printer deposits binder in 'core-shell' mode by default, the concentration gradient tends to be distributed uniformly in the just-printed contour, immediately after deposition on the powder surface. As a result, the core-shell effect was noticed to be less in a printed contour. Another limitation of moisturised powder is the formation of agglomerated flow during spreading, resulting in macropores in the layers. The accumulation of these macropores in subsequent layers is detrimental for the microstructure, which can lead to premature failure under mechanical forces.

In an attempt to avoid moisturising the powder and at the same time achieving cohesive bed packing, zirconia was blended with zirconium silicate (zircon). The reactivity of APS modified zircon-zirconia blend with the binder to trigger the polymerisation is consistent even after preservation for a long time (in months). This endorses the effectiveness of silicate blending to achieve cohesive bed pack compared to 'controlled humidification'. The schematic representation for the rationale of partial humidification and metal silicate blending is provided in Figure S4. Using a novel 'dual deposition' strategy, first coined in this study (Figure S1), it is also made possible to wave away the macroporous layers during powder spreading and achieving smooth layers for printing.

4.2. Machine limited 'core-shell' mode of printing and post-processing

It is sufficiently addressed previously that the commercial printer (Projet 460 plus, 3D Systems) adopts the 'default' core-shell mode of binder/ink deposition, 'overriding' any command to change or homogenise the saturation from shell to core. The adverse effect is visible in the printed-sintered architectures of zircon-zirconia based bioceramics. The densification is so less at the core that after fracture of the sintered structure (under uniaxial compressive or flexural load), unbound powder could be found at the core region. This was even visible after 3 cycles of infiltration-conversion and high temperature sintering (1450 °C). The unbound powder particles are also observed in the core area of zirconia and ZTA based bioceramics, although the extent is lesser than the zircon-zirconia system due to the presence of the moisture content in the powder. The moisture content assisted in homogenising the segregated binder saturation from shell to core in each layer. If the powder particles do not bind intimately in the green body itself (especially in the core) during binderjet printing, it is difficult to make them compact by pressureless sintering. Another adverse effect of the 'infiltration-conversion' to fill up the micropores in the structure is the transformation of the tetragonal zirconia to the monoclinic phase. The *in situ* converted tetragonal zirconia (from zirconyl oxychloride) is unstabilized. As a result, after high temperature sintering (1450 °C) and subsequent cooling to room temperature, the tetragonal phase converted to higher

volumetric monoclinic phase. This leads to cracks formation both in the body and the surfaces (Fig. 9), leading to premature/unpredicted failure under different types of loading. This effect is schematically depicted in Fig. 12.

Another strategy was adapted to infiltrate the as-printed bodies with the parent binder. As the unbound powder particles in the as-printed parts contain the partially unreacted APS initiator, the acrylic binder still can polymerise and consolidate the unbound particles. Unfortunately, this strategy also did not work to make dense green bodies. After the infiltration of the as-printed bodies with acrylic binder, large voids were created inside the body, because of initial loose packing in the core region. The shell, being well bonded and stiffer, did not respond to the infiltration, but the highly porous core got compacted by binder infiltration and polymerisation, leading to the detachment from the shell. This leaves larger pores/holes between the shell and the infiltration induced compacted core. Unpredicted/catastrophic failure can occur under load application, due to these structural defects.

From the above experimental analysis and scientific hypothesis wherever applicable, it is now apparent that the final barrier to achieve homogeneous microstructure and uncompromised mechanical properties is to overcome the machine limited 'core-shell' mode of printing. As per the current knowledge where it is not known how to stop/bypass the 'default core-shell mode of printing', we shall discuss the suitable troubleshooting methodologies to overcome such limitations at the end of this section.

4.3. Morphology, densification and mechanical properties

'Processing-microstructure-property' is the theme of biomaterials science and engineering in strategic designing of product manufacturing, where all the three stages are interactive and feedback dependent. Discrete microstructures evolve from different processing approaches, dictating the desired functional or structural properties.

The dense and compact grain structure of zirconia and ZTA represents the morphology of the 'material islands' of the shell region. All the material islands are connected with each other through highly interconnected 3D microporosities. It is not expected to have the similar kind of grain structure at the core of the 3D printed ceramics, where the particles are found to be visually unbound and not densified at all. It is therefore implicative that, if the core region would be printed with same saturation as the shell, similar dense grain structure could be anticipated at the core region as well. The compact grain structures of the binderjet printed-sintered bioceramic materials endorse the efficacy of the binder system to print bioceramic materials, apart from metallic biomaterial, Ti-6Al-4V²². The extensive presence of the interconnected capillaries are expected to be originated from the random presence of macropores in each layer during printing, where in the 'first generation' approach, 'dual deposition' was not available to ensure smoother layers (Fig. 3). Albeit, the interconnected porosities cannot be fully avoided during powder bed based binderjet printing methodology, which is beneficial for biomedical applications.

As the density is a 'bulk/intensive' property of a solid ceramic, consistent lower values of apparent densities (slightly higher than half

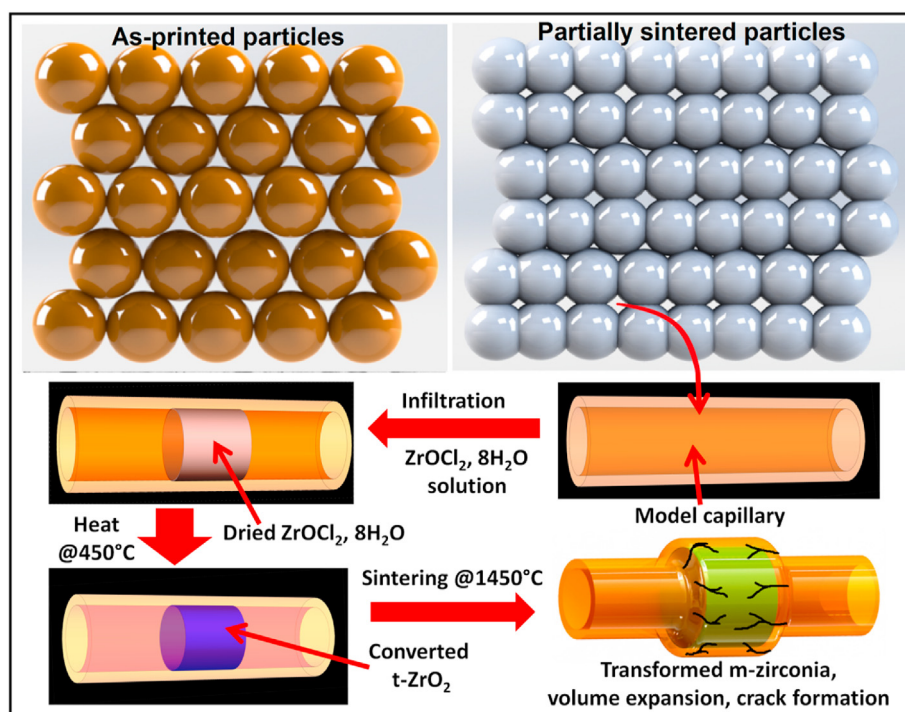


Fig. 12. Schematic illustration of ‘infiltration-conversion-sintering’ based post-processing to compensate the as-printed microporosity. Being unstable in nature, the converted $t\text{-ZrO}_2$ (@450 °C from infiltrated-dried $\text{ZrOCl}_2, 8\text{H}_2\text{O}$) when sintered at 1450 °C and cooled down to room temperature, gets transformed to $m\text{-ZrO}_2$. As a result, the volume expands leading to crack formation in the as-sintered body.

the values of the corresponding true densities) signify the inefficient densification, which is anticipated from the unbound powder particles comprising the bulk solid ($\geq 80\%$ of the entire volume), i.e. the ‘core’. The high volume porosities ($\sim 40\%$ from He-gas pycnometry) in all the final sintered zirconia, zircon-zirconia and ZTA parts further endorse the significantly lower density and mechanical properties. The high porosity in the as-printed green bodies (not measured but at least 10% higher than the sintered ones, i.e. $\geq 50\%$) originated from the loosely bonded bulk body (core) and macroporous layers (first generation) deposition during printing. These limitations can be addressed by intelligently bypassing/restricting the ‘core-shell’ mode of printing and ‘dual deposition’ (second generation) of powder in order to achieve non-macroporous layers.

As discussed above, the core-shell mode of printing leaves a permanent adverse effect on the microstructure with an unwanted gradient in the particle arrangements from the shell to core. It is also highlighted that the mechanical properties, be it compressive, flexural, or tensile strength, should be contributed by the evolution of microstructure during the entire processing cycle. As the binderjet printed-post processed-sintered bioceramics still possess the core-shell gradient in the structure, the load is borne by only the thin shell and no contribution is experienced by the loosely bonded core. As a result, when the shell breaks, the cracks propagate through the core without any resistance and the body collapses instantly. The modest compressive, tensile, and flexural strengths are the inevitable outcomes of this structural limitation.

It was observed that, although counterintuitively, the flexural strengths were higher than the compressive strengths of the 3D printed-sintered architectures. This can be attributed to the core-shell structure. In compression test, once the top shell encountering the moving top platen fractures, there is no supporting dense structure inside the body to withstand the load. As a result, the ceramics collapse under compression rapidly. But in case of 3-point bend tests, two shells act together to counter the bending load from both top surface (compressive) and bottom surface (tensile), making it comparatively stronger and more reliable than the uniaxial compressive and diametral compression tests. This effect is observed in a high flexural Weibull modulus (>9) although the

mean strength values are less (~ 12 MPa). This confirms the consistency in the results and more reliability in the strength properties in the flexural mode of loading applications. The explanation of the anomalous behaviour (higher flexural strength than compressive strength) is illustrated in Fig. 10c. The presence of lesser extent of ‘core-shell’ in the zirconia architectures made from partially humidified powder (first generation modification), the reliability of compressive strength was commendable (Weibull modulus >9).

Although the printing-induced ‘core-shell’ gradient in the microstructure remains the foremost player accounted for inferior mechanical properties, another factor for the poor mechanical properties in zircon-zirconia system is contributed by the monoclinic zirconia formation in as-sintered microstructure. As discussed, the infiltrated zirconyl chloride converts to tetragonal zirconia at 450 °C and when sintered at 1450 °C and cooled down to room temperature, the unstabilized ZrO_2 got transformed to the monoclinic phase (Fig. 12). The monoclinic phase is volumetrically larger than the tetragonal phase and mechanically inferior. As a result, surface cracks were noticed in the final sintered architectures reducing the mechanical properties further. In addition, it is worthwhile to reiterate here that, the poor mechanical properties of zirconia and ZTA are associated with the macroporous layer deposition during printing and ‘core-shell’ microstructure. To troubleshoot the limitations of 3D binderjet printing of ceramic biomaterials for biomedically relevant structural applications using the commercial machine (e.g. ProJet 460 plus, 3D systems), alternative methodologies should be considered. These are the potential areas of extended future work.

5. Conclusions

In this work, extensive endeavors of 3D binderjet printing of ceramic-based biomaterials are depicted, where the applicability of the novel acrylic based ink/binder is established with modest success due to machine limitation. 3 mol% YSZ, powder blends of zirconia-alumina (3:22, wt/wt) and zircon-zirconia (1:3, wt/wt) was proved to be printable and a ‘dual deposition’ methodology was innovated to address the limitation in

zircon-zirconia system. Multistage sintering for zirconia and ZTA was adapted and a new approach of ‘pre-sintering – zirconium salt infiltration – phase conversion – full sintering’ was introduced to allow *in situ* formation of zirconia in the micropores of partially sintered architectures. XRD analysis revealed the stability of the silicate in the final sintering temperature which also endorsed the tetragonal phase of the converted zirconia from the infiltrated zirconium salt. The microstructure is characterized by compact grain structures of zirconia and ZTA in the ‘shell’ region, while the powder particles remained unbound at the ‘core’ due to ‘default half saturation’ granted during binderjet printing. In addition to the poor bonding and inferior densification, large microcracks were observed in the ‘core’ regions of the final sintered bioceramics, which adversely impacted the mechanical properties. Weakest link fracture statistics revealed good flexural strength reliability of zircon-zirconia system and compressive strength reliability of zirconia (Weibull modulus for both >9), although the mean strengths remained significantly low. The inferior mechanical properties were attributed to the structural heterogeneity evolved from the ‘machine limited core-shell’ mode of printing, leading to premature failure of the parts under compression/flexural mode. Future experimental researches should be designed to address these limitations either by modifying the powder further or altering the CAD designs.

Acknowledgement

The authors would like to acknowledge Department of Science and Technology (DST), Department of Biotechnology (DBT) (grant no. BT/PR13466/COE/34/26/2015), Government of India, and Centres of Excellence and Innovation in Biotechnology – ‘Translational Center on Biomaterials for Orthopaedic and Dental Applications’ for financial supports.

Appendix A. Supplementary data

Supplementary data to this article can be found online at <https://doi.org/10.1016/j.oceram.2020.100026>.

References

- [1] S. Barui, S. Mandal, B. Basu, Thermal inkjet 3D powder printing of metals and alloys: current status and challenges, *Current Opinion in Biomedical Engineering* 2 (2017) 116–123.
- [2] U. Gbureck, et al., Resorbable dicalcium phosphate bone Substitutes prepared by 3D powder printing, *Adv. Funct. Mater.* 17 (2007) 3940–3945.
- [3] F.P.W. Melchels, et al., Additive manufacturing of tissues and organs, *Prog. Polym. Sci.* 37 (2012) 1079–1104.
- [4] S. Bose, S. Vahabzadeh, A. Bandyopadhyay, Bone tissue engineering using 3D printing, *Mater. Today* 16 (2013) 496–504.
- [5] A. Kumar, et al., Low temperature additive manufacturing of three dimensional scaffolds for bone-tissue engineering applications: processing related challenges and property assessment, *Mater. Sci. Eng. R Rep.* 103 (2016) 1–39.
- [6] A. Kumar, et al., Low temperature additive manufacturing of three dimensional scaffolds for bone-tissue engineering applications: processing related challenges and property assessment, *Mater. Sci. Eng. R Rep.* 103 (2016) 1–39.
- [7] J. Chevalier, What future for zirconia as a biomaterial? *Biomaterials* 27 (2006) 535–543.
- [8] J.R. Kelly, I. Denry, Stabilized zirconia as a structural ceramic: an overview, *Dent. Mater.* 24 (2008) 289–298.
- [9] L. Ferrage, G. Bertrand, P. Lenormand, D. Grossin, B. Ben-Nissan, A review of the additive manufacturing (3DP) of bioceramics: alumina, zirconia (PSZ) and hydroxyapatite, *J. Australian Ceramic Soc.* 53 (2017) 11–20.
- [10] A. Ghazanfari, W. Li, M.C. Leu, J.L. Watts, G.E. Hilmas, Additive manufacturing and mechanical characterization of high density fully stabilized zirconia, *Ceram. Int.* 43 (2017) 6082–6088.
- [11] H. Shao, D. Zhao, T. Lin, J. He, J. Wu, 3D gel-printing of zirconia ceramic parts, *Ceram. Int.* 43 (2017) 13938–13942.
- [12] U. Scheithauer, E. Schwarzer, H.-J. Richter, T. Moritz, Thermoplastic 3D printing—an additive manufacturing method for producing dense ceramics, *Int. J. Appl. Ceram. Technol.* 12 (2015) 26–31.
- [13] K. Shahzad, J. Deckers, Z. Zhang, J.-P. Kruth, J. Vleugels, Additive manufacturing of zirconia parts by indirect selective laser sintering, *J. Eur. Ceram. Soc.* 34 (2014) 81–89.
- [14] J. Wilkes, Y.C. Hagedorn, W. Meiners, K. Wissenbach, Additive manufacturing of ZrO₂-Al₂O₃ ceramic components by selective laser melting, *Rapid Prototyp. J.* 19 (2013) 51–57.
- [15] Z. Fan, Y. Zhao, M. Lu, H. Huang, Ytria stabilized zirconia (YSZ) thin wall structures fabricated using laser engineered net shaping (LENS), *Int. J. Adv. Manuf. Technol.* 105 (2019) 4491–4498.
- [16] S. Yan, et al., 3D printing of nano-scale Al₂O₃-ZrO₂ eutectic ceramic: Principle analysis and process optimization of pores, *Additive Manufacturing* 28 (2019) 120–126.
- [17] R. He, et al., Fabrication of complex-shaped zirconia ceramic parts via a DLP-stereolithography-based 3D printing method, *Ceram. Int.* 44 (2018) 3412–3416.
- [18] H. Wu, et al., Fabrication of dense zirconia-toughened alumina ceramics through a stereolithography-based additive manufacturing, *Ceram. Int.* 43 (2017) 968–972.
- [19] S. Meininger, et al., Strength reliability and in vitro degradation of three-dimensional powder printed strontium-substituted magnesium phosphate scaffolds, *Acta Biomater.* 31 (2016) 401–411.
- [20] S. Mandal, S. Meininger, U. Gbureck, B. Basu, 3D powder printed tetracalcium phosphate scaffold with phytic acid binder: fabrication, microstructure and in situ X-Ray tomography analysis of compressive failure, *J. Mater. Sci. Mater. Med.* 29 (2018) 29.
- [21] S. Mandal, B. Basu, Probing the influence of post-processing on microstructure and in situ compression failure with in silico modeling of 3D-printed scaffolds, *J. Mater. Res.* 33 (2018) 2062–2076.
- [22] S. Barui, et al., 3D inkjet printing of biomaterials with strength reliability and cytocompatibility: Quantitative process strategy for Ti-6Al-4V, *Biomaterials* 213 (2019) 119212.
- [23] A.M. Wätjen, P. Gingter, M. Kramer, R. Telle, Novel Prospects and Possibilities in additive manufacturing of ceramics by means of direct inkjet printing, *Adv. Mech. Eng.* 6 (2014) 141346.
- [24] J. Ebert, et al., Direct inkjet printing of dental Prostheses made of zirconia, *J. Dent. Res.* 88 (2009) 673–676.
- [25] E. Özkol, W. Zhang, J. Ebert, R. Telle, Potentials of the “Direct inkjet printing” method for manufacturing 3Y-TZP based dental restorations, *J. Eur. Ceram. Soc.* 32 (2012) 2193–2201.
- [26] N. Ramakrishnan, P.K. Rajesh, P. Ponnambalam, K. Prakasan, Studies on preparation of ceramic inks and simulation of drop formation and spread in direct ceramic inkjet printing, *J. Mater. Process. Technol.* 169 (2005) 372–381.
- [27] R. Dou, T. Wang, Y. Guo, B. Derby, Ink-jet printing of zirconia: coffee staining and line stability, *J. Am. Ceram. Soc.* 94 (2011) 3787–3792.
- [28] A. Budding, T.H.J. Vaneker, A.J.A. Winnubst, Open Source powder based rapid prototyping machine for ceramics, *Procedia CIRP* 6 (2013) 533–538.
- [29] S. Huang, C. Ye, H. Zhao, Z. Fan, Q. Wei, Binder jetting yttria stabilised zirconia ceramic with inorganic colloid as a binder, *Advances in Applied Ceramics* 118 (2019) 458–465.
- [30] R.K. Holman, M.J. Cima, S.A. Uhland, E. Sachs, Spreading and infiltration of inkjet-printed polymer solution Droplets on a porous substrate, *J. Colloid Interface Sci.* 249 (2002) 432–440.
- [31] A. Mostafaei, et al., Powder bed binder jet printed alloy 625: densification, microstructure and mechanical properties, *Mater. Des.* 108 (2016) 126–135.
- [32] P. Nandwana, et al., Powder bed binder jet 3D printing of Inconel 718: densification, microstructural evolution and challenges☆, *Curr. Opin. Solid State Mater. Sci.* 21 (2017) 207–218.
- [33] S. Barui, et al., Probing ink-powder interactions during 3D binderjet printing using time resolved X-ray imaging, *ACS Applied Materials & Interfaces*, 2020.